The 12th International Conference on Motion and Vibration
MOVIC2014

3D13

Actuator control for a rapid prototyping railway bogie, using a dynamically substructured systems approach

Nobuyuki WATANABE* and David P. STOTEN**
*Railway Technical Research Institute
2-8-38 Hikaricho, Kokubunji-shi, Tokyo, 185-8540, Japan
E-mail: watanabe.nobuyuki.53@rtri.or.jp
**Advanced Control & Test Laboratory (ACTLab), Department of Mechanical Engineering, University of Bristol
Queen's Building, University Walk, Bristol, BS8 1TR, United Kingdom

Abstract
In this paper we present a method of improving actuator control performance of a rapid prototyping bogie (RPB), which has 9 electric actuators. The actuators emulate missing railway bogie suspension components and are used to determine an optimal parameter set for them via a test bench system. In the original RPB hybrid control system, the actuators were force-controlled independently of each other, according to the behaviour of a virtual suspension model. During the RPB performance tests deterioration in the control performance was observed, which was caused by dynamic coupling between the multiple actuators. To solve this issue, we have developed a new controller based upon the dynamically substructured systems (DSS) method, which ensures accurate synchronisation of numerical and physical states at their common boundaries. A description of this DSS approach applied to the RPB problem therefore forms the core of this paper. To confirm the effectiveness of the new approach, we implemented a DSS-based controller into an existing proof-of-concept test rig, which has characteristics that are common to the RPB - in particular, it has multiple actuators attached to the same rigid body component and the existence of rubber bushes to protect the actuators from excessive bending moments. A simplified, linear model of a single railway wheel-set system was chosen as an example. Each actuator emulates not only a virtual primary suspension but also virtual creep forces. A state-space DSS approach was adopted to improve numerical conditioning. Through random excitation tests with the DSS controller, we confirmed that the actuators were well synchronized with their numerical models and that the previously observed and unexpected frequency components were removed. As a consequence, the DSS approach was determined as a viable framework for future research on the RPB system.

Keywords : Hybrid Testing, Rapid Prototyping Bogie, Dynamically Substructured Systems, Automatic Control, State-Space Methods, Dynamic Coupling, Railway Vehicle Design

1. Introduction

Rapid prototyping is a form of advanced testing, the concepts of which are now receiving more interest in product design. In rapid prototyping tests, actuators substitute for missing components and, with suitable control, can emulate their characteristics. This enables the evaluation of product performance under virtually real conditions before manufacturing the final product, not only reducing time and cost by omitting the prototyping stage, but also improving quality by allowing more time for testing. Using this technique, the Railway Technical Research Institute (RTRI) in Japan has developed a rapid prototyping bogie (RPB) (Morishita, et al., 2010). The RPB has 9 electrical actuators to substitute for missing railway bogie suspension components, and its purpose is to determine an optimal parameter set for them on the rolling stock test plant (RSTP) at RTRI.

Thus, the original RPB controller was based upon a hybrid testing technique using numerical (virtual suspension) models and physical components (actuators and other bogie components). The technique was deemed suitable for the RPB because it was straightforward to change the characteristics of virtual suspensions by simply replacing numerical models of them. The actuators were force-controlled independently of each other, according to the behaviour of a

virtual suspension device model (i.e. a reference model). Although the controller was adequate under the condition that each actuator was independently shaken, unexpected high frequency components were observed in the RPB performance tests (Watanabe, et al., 2012). It was concluded that dynamic coupling between the multiple actuators caused this deterioration in the control performance of the RPB and that a more effective technique was required.

In more recent years, a new form of mixed physical-numerical strategy has been developed, called the dynamic substructuring system testing method (or DSS, for short), which is an alternative to hybrid testing. Although it is more complicated to design than the hybrid test system, DSS has the significant advantage of ensuring stable and accurate synchronisation of multi-axis numerical and physical substructures at their common boundaries, even in the face of dynamic uncertainty. One of the first of this new type was described in (Stoten and Hyde, 2006), which allowed for linear or adaptive algorithms (or a combination thereof) in the process of controlled synchronisation. A description of this DSS approach applied to the RPB problem therefore forms the core of this paper.

The rest of this paper is structured as follows. An outline of the RPB is presented in section 2, including observed issues in the previous tests. In section 3, implementation tests using the existing proof-of-concept rig are described. Although components of this rig are different from those of the RPB, a similar single wheel-set model and appropriate parameter sets of the virtual device are used. Therefore the rig tests are fundamentally similar to those used on the RPB. Controlled performance comparisons are conducted via simulations in section 4. Finally, section 5 draws together the main conclusions from this work.

2. Overview of the original RPB scheme at RTRI

2.1 RPB system

The RPB, shown in Fig. 1, has 9 electric actuators: (a) 4 longitudinal actuators for longitudinal axle box stiffness, (b) 2 anti-yawing actuators, (c) 2 vertical actuators for vertical stiffness of the air springs and (d) 1 lateral actuator representing the lateral damping and stiffness of the air springs. Actuators in (a) and (b) substitute directly for the corresponding bogie suspension components, and the others compensate for existing suspensions, such as air springs, for emulating the characteristics of the missing suspensions.

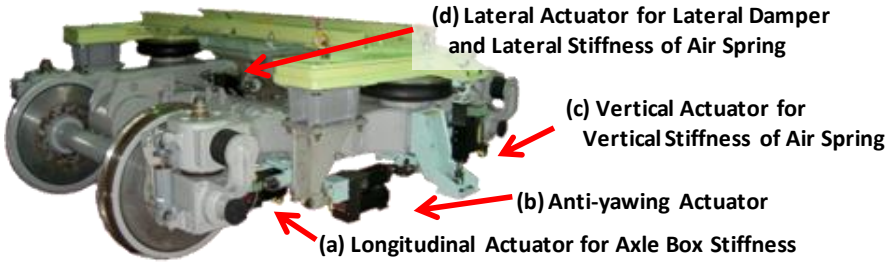

Fig. 1 Overview of the RPB

Under normal straight-track conditions, motions of axle boxes in the longitudinal direction, together with the stroke amplitudes of anti-yawing dampers, are less than 1mm. Their characteristics have a significant effect on bogie stability; therefore any gaps at points of attachment should be avoided. Nevertheless, the RPB actuators require some protection from excessive bending moments. To cope with these demands, crossed roller bearings and rubber bushes are used at the ends of actuators in (a) and (b), above. Figure 2 shows an anti-yawing actuator with a bending moment protection mechanism. The controller can acquire actuator displacement and force outputs via a servo-motor rotational encoder and load cell, but cannot directly access rubber deformation information, due to the lack of a suitable sensor.

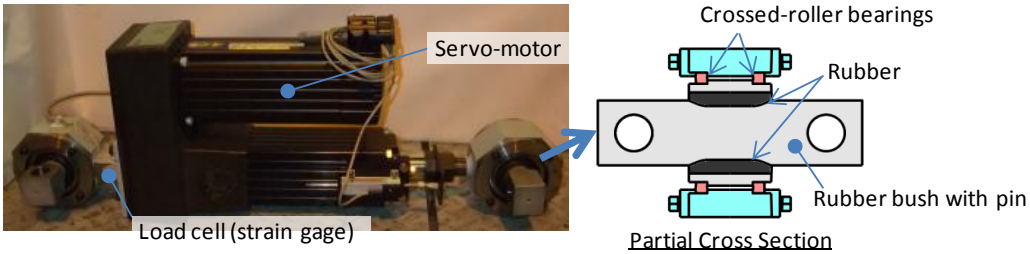

Fig. 2 Overview of anti-yawing actuator

2.2 Hybrid controller

As described above, in the original RTRI scheme the actuators were force-controlled independently of each other using a hybrid scheme, according to the output of the corresponding reference model; see Fig. 3. The external controller was built using Matlab Simulink and xPCTarget. Each fixed feedback gain was determined via independent shaking tests.

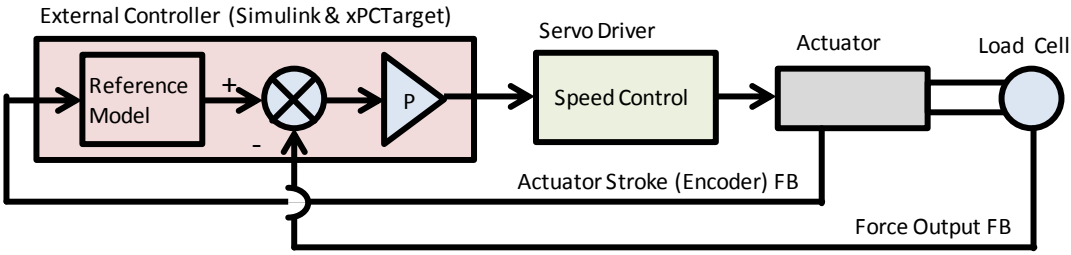

Fig. 3 Hybrid controller diagram for the RPB actuator

2.3 Original RPB tests

Figure 4 shows a single test-bench shaking test result, together with a RSTP performance test result conducted on a longitudinal actuator. The force output tracked the demand with sufficient accuracy when the actuator was shaken independently. However there were two unexpected peaks in the power spectral density (PSD) curve at 7.7Hz and 14Hz, which were beyond the frequency bandwidth of the roller rig excitation. Note that the running speed of the performance test was 50km/h; therefore the RPB should remain in a stable condition. Consequently, it was concluded that dynamic coupling between the multiple actuators caused this deterioration in the hybrid control performance.

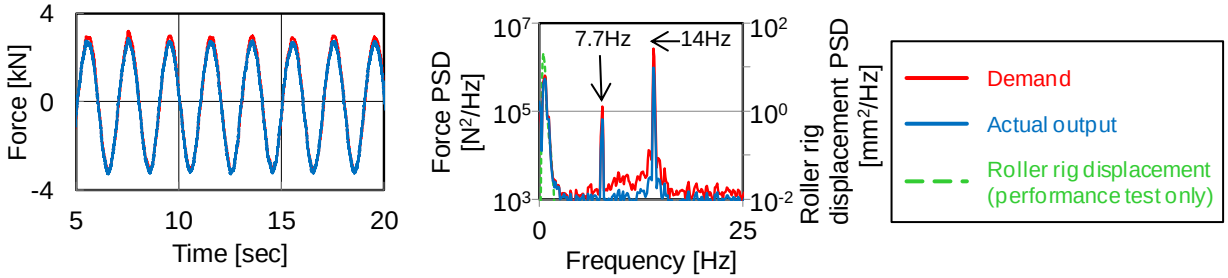

(a) Independently shaken test at test bench (b) Performance test in RSTP

Fig. 4 Demand force and actual output one of a longitudinal actuator. In the 0.5Hz sinusoidal, independently shaken test, the actual output tracked demand. However, in the RSTP random excitation test, dynamic coupling caused both demand and actual output to have high frequent components at 7.7Hz and 14Hz, which were beyond roller rig displacement (excitation) component bandwidth.

3. DSS implementation study using an existing test rig

In this study, our objective was to investigate if DSS was a viable framework for the RPB in the following two respects: (1) avoid any deterioration of control performance caused by dynamic coupling and (2) ensure straightforward parameter changeability of the virtual elements. Therefore, we constructed the laboratory test system using an existing rig in Bristol University's ACTLab and then implemented the corresponding DSS controllers. In this section, we describe the rig and the emulation model, details of DSS controller design and present the key results from the shaking tests.

3.1 Outline of the new test rig and the emulation model

The ACTLab test rig and its developed schematic form are shown in (Fig. 5). The rig consists of 2 hydraulic actuators, 2 suspension units, 1 rigid body beam and a dSPACE DSP control system. This rig was chosen as a viable proof-of-concept since it has characteristics that are common to the RPB - in particular, it has multiple actuators attached to the same rigid body component and the existence of rubber bushes to protect RPB actuators from excessive

bending moments.

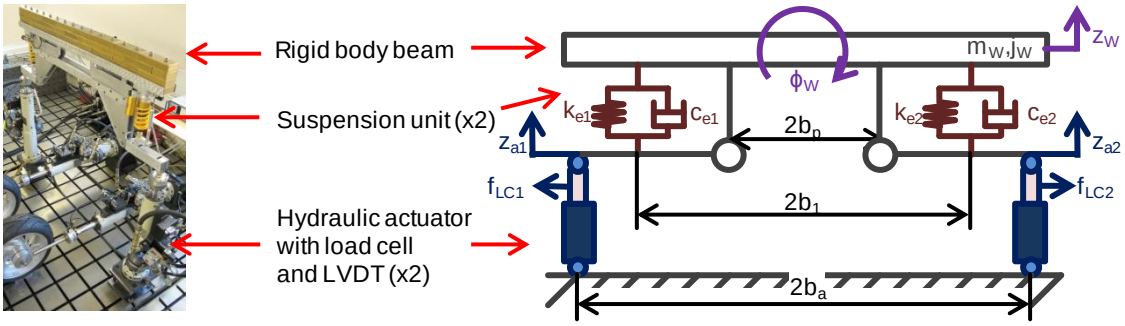

Fig. 5 Proof-of-concept test rig showing 2 hydraulic actuators, 2 suspension units and 1 rigid body. On the left is the actual system and on the right is its schematic representation.

This demonstrator system was a simplification of the actual RPB used by the RSTP. Typically, the RPB is shaken in the lateral direction by roller rigs and a creep force, a form of friction between wheel and rail, which affects the wheel-set motion (Fig. 6(b)). Although creep force is a non-linear phenomenon in theory, linear approximations can be applied in the case of small relative motion between wheel and rail. The demonstrator model (Fig. 6(a)) was designed so that it represented a wheel-set supported by 2 primary suspensions and shaken vertically via 2 creep-dampers. The corresponding linearised equations of the model are given by Eq. (1) and (2).

In the laboratory test system, each suspension unit was regarded as part of the corresponding hydraulic actuator and each actuator of the rig emulated not only a virtual primary suspension but also virtual creep force.

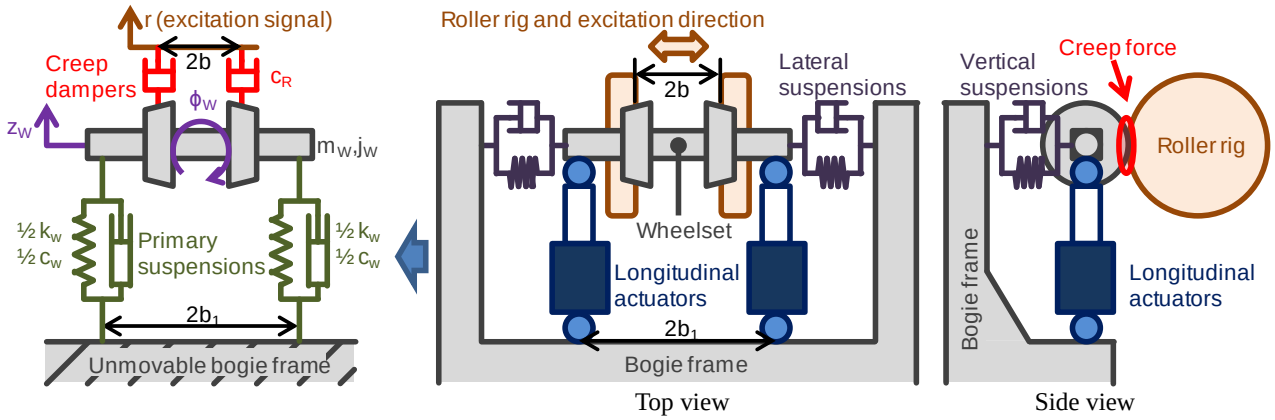

(a) Demonstrator model (b) Typical usage of longitudinal actuators at the RSTP

Fig. 6 Demonstrator model and typical usage of RPB at the RSTP. In the model, the bogie frame is fixed and lateral and vertical suspensions are omitted. In addition, the creep force is represented via the action of linear creep-dampers.

$$m_w \ddot{z_w} + c_w \dot{z_w} + k_w z_w = 2c_R(\dot{r} - \dot{z_w}) \quad (1)$$

$$j_w \ddot{\phi_w} + b_1^2 c_w \dot{\phi_w} + b_1^2 k_w \phi_w = -2b^2 c_R \dot{\phi_w} \quad (2)$$

3.2 Controller design

In this research, the variables to be synchronised by the DSS controller were the numerical model and actual actuator displacements. This implied that the measured force was treated as an input and the demanded actuator displacement as an output, which was the opposite of the case with the original RPB controller, being introduced for reasons of experimental convenience. Although the original transfer function DSS approach resulted in successful performance using the same ACTLab rig in previous work (Stoten, et. al., 2009), the state-space DSS approach by the same authors (Tu, et. al., 2009) was adopted. We note that the synchronising controller of the transfer function based approach is generally of high order and if applied to the RPB (which is more complex dynamically than the ACTLab rig), numerical conditioning could be a problem.

3.2.1 The state-space DSS approach

Figure 7 shows the framework of the state-space DSS approach based on (Tu, et. al., 2009). Here, the entire emulated system is decomposed into two substructures, $\{\Sigma_N, \Sigma_P\}$; Σ_N is the numerical substructure, Σ_P is the physical one. Σ_1 in Σ_N is related to the characteristics of numerically emulated components, Σ_2 in Σ_P to the dynamics of physical test components, and G_{TS} in Σ_P to the transfer system of actuators. In this study, the corresponding dynamic elements are the virtual primary suspensions and creep-dampers, the rigid beam and suspension units, and the hydraulic actuators, respectively. The interaction term between Σ_P and Σ_N, y_i, is a vector of the measured forces f_{LC1} and f_{LC2}. z_P and z_N are the physical and numerical outputs to be synchronised. Actuator displacements are the outputs in this study. Note that in Fig. 8, $\dot{r}$ is used as the reference input, since the transfer function from reference to state variables must be strictly proper in order to formulate the subsequent developments in section 3.2.3. Replacing r by $\dot{r}$ is not a serious problem, since this excitation signal is always known in advance in DSS testing, so that $\dot{r}$ can be determined *a priori*.

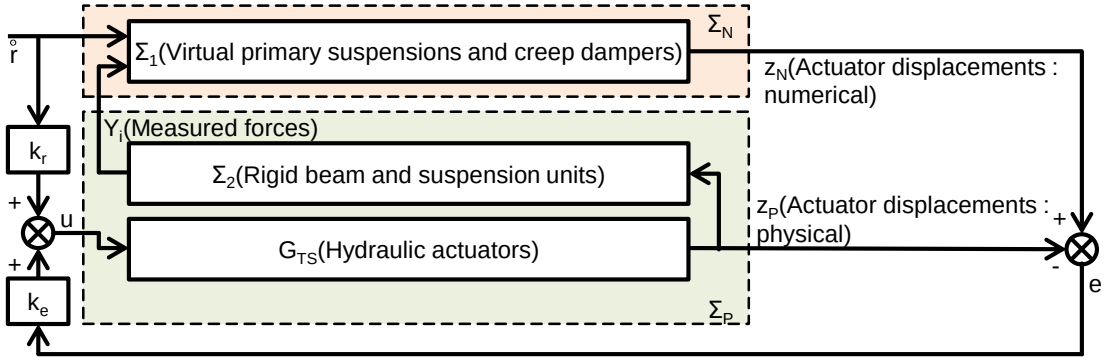

Fig. 7 The DSS framework based on reference (Tu, et. al., 2009). Gains k_r and k_e are determined so as to synchronize the numerical and physical outputs z_N and z_P. The corresponding dynamic elements in this study are shown in parentheses.

Assuming that state variables of Σ_N and Σ_P contain the synchronizing variables z_N and z_P, respectively, the state and output equations can be written as:

$$\Sigma_N: \begin{pmatrix} \dot{z_N} \\ \dot{z_{N2}} \end{pmatrix} = \begin{pmatrix} A_{N11} & A_{N12} \\ A_{N21} & A_{N22} \end{pmatrix} \begin{pmatrix} z_N \\ z_{N2} \end{pmatrix} + \begin{pmatrix} B_{Ni} \\ B_{Ni2} \end{pmatrix} y_i + \begin{pmatrix} B_{Nr} \\ B_{Nr2} \end{pmatrix} \dot{r} \tag{3}$$

$$z_N = (I \quad 0) \begin{pmatrix} z_N \\ z_{N2} \end{pmatrix} \tag{4}$$

$$\Sigma_P: \begin{pmatrix} \dot{z_P} \\ \dot{z_{P2}} \end{pmatrix} = \begin{pmatrix} A_{P11} & A_{P12} \\ A_{P21} & A_{P22} \end{pmatrix} \begin{pmatrix} z_P \\ z_{P2} \end{pmatrix} + \begin{pmatrix} B_{Pu} \\ B_{Pu2} \end{pmatrix} u \tag{5}$$

$$z_P = (I \quad 0) \begin{pmatrix} z_P \\ z_{P2} \end{pmatrix} \tag{6}$$

$$y_i = (C_{Pi1} \quad C_{Pi2}) \begin{pmatrix} z_P \\ z_{P2} \end{pmatrix} + D_{Pi} u \tag{7}$$

where z_{N2} and z_{P2} are subsets of the state variables of Σ_N and Σ_P, respectively; see Eq. (3) ~ (6). Note that All matrices are decomposed into submatrices which have corresponding dimensions of the synchronizing variables and their subsets. From Eq. (3) ~ (7), the state equation of the synchronized error $e = z_N - z_P$ is derived as follows:

$$\begin{aligned} \dot{e} = \dot{z_N} - \dot{z_P} &= \left\{ (A_{N11} \quad A_{N12}) \begin{pmatrix} z_N \\ z_{N2} \end{pmatrix} + B_{Ni} y_i + B_{Nr} \dot{r} \right\} - \left\{ (A_{P11} \quad A_{P12}) \begin{pmatrix} z_P \\ z_{P2} \end{pmatrix} + B_{Pu} u \right\} \\ &= A_{N11} e + A_{N12} z_{N2} + (A_{N11} + B_{Ni} C_{Pi1} - A_{P11}) z_P + (B_{Ni} C_{Pi2} - A_{P12}) z_{P2} + (B_{Ni} D_{Pi} - B_{Pu}) u + B_{Nr} \dot{r} \end{aligned} \tag{8}$$

Therefore, assuming that the controllability matrix $[(B_{Ni}D_{Pi}-B_{Pu}) \quad (B_{Ni}D_{Pi}-B_{Pu})A_{N11}]$ is of full rank (e is a 2×1 vector) and that all state variables can be measured, the following control input vector u ensures that $e \to 0$:

$$u = -(B_{Ni}D_{Pi}-B_{Pu})^{-1}A_{N11}e - (B_{Ni}D_{Pi}-B_{Pu})^{-1}A_{N12}z_{N2} - (B_{Ni}D_{Pi}-B_{Pu})^{-1}(A_{N11}+B_{Ni}C_{Pi1}-A_{P11})z_P \\ -(B_{Ni}D_{Pi}-B_{Pu})^{-1}(B_{Ni}C_{Pi2}-A_{P12})z_{P2} - (B_{Ni}D_{Pi}-B_{Pu})^{-1}B_{Nr}\dot{r} \tag{9}$$

The first term on the right-hand side of Eq. (9) is the error feedback term $k_e e$ in Fig. 7, and the remainder of the terms constitute the feedforward term $k_r\dot{r}$. In this study, all state variables including z_P can be obtained numerically in order to calculate $k_r\dot{r}$.

3.2.2 Equations of motion and actuator dynamics

In this section, capital letters represent Laplace-transformed variables, e.g. Z_w is the Laplace transformed variable of z_w. Considering that the measured forces F_{LC1} and F_{LC2}, which are obtained from load cells attached in hydraulic actuators (see Fig. 5), are positive in tension, we obtain:

$$\begin{pmatrix}F_{LC1}\\F_{LC2}\end{pmatrix} = -\gamma\begin{pmatrix}g_{e1}\gamma(Z_{a1}-Z_w-b_a\Phi_w)\\g_{e2}\gamma(Z_{a2}-Z_w+b_a\Phi_w)\end{pmatrix} = -\gamma^2\begin{pmatrix}g_{e1}&0\\0&g_{e2}\end{pmatrix}\begin{pmatrix}Z_{a1}\\Z_{a2}\end{pmatrix} + \gamma^2\begin{pmatrix}g_{e1}&b_ag_{e1}\\g_{e2}&-b_ag_{e2}\end{pmatrix}\begin{pmatrix}Z_w\\\Phi_w\end{pmatrix} \tag{10}$$

where g_{e1} and g_{e2} are characteristics of the rig suspension units, and γ is the arm-lever ratio of the suspension unit given by $g_{e1}=c_{e1}s+k_{e1}$, $g_{e2}=c_{e2}s+k_{e2}$, and $\gamma=(b_1-b_p)/(b_a-b_p)$, respectively. In addition, F_{LC1} and F_{LC2} represent external forces which affect the beam dynamics. In this model, these forces are equal to the outputs of virtual primary suspensions and creep-dampers and are therefore also given by:

$$\begin{pmatrix}-1&-1\\-b_a&b_a\end{pmatrix}\begin{pmatrix}F_{LC1}\\F_{LC2}\end{pmatrix} = -\begin{pmatrix}(2c_R+c_w)s+k_w&0\\0&(2b^2c_R+b_1^2c_w)s+b_1^2k_w\end{pmatrix}\begin{pmatrix}Z_w\\\Phi_w\end{pmatrix} + \begin{pmatrix}2c_Rs\\0\end{pmatrix}R \\ \therefore \begin{pmatrix}Z_w\\\Phi_w\end{pmatrix} = \begin{pmatrix}\frac{1}{\alpha}&0\\0&\frac{1}{\beta}\end{pmatrix}\begin{pmatrix}1&1\\b_a&-b_a\end{pmatrix}\begin{pmatrix}F_{LC1}\\F_{LC2}\end{pmatrix} + \begin{pmatrix}\frac{1}{\alpha}&0\\0&\frac{1}{\beta}\end{pmatrix}\begin{pmatrix}2c_Rs\\0\end{pmatrix}R \tag{11}$$

where $\alpha=(2c_R+c_w)s+k_w$, $\beta=(2b^2c_R+b_1^2c_w)s+b_1^2k_w$. From Eq. (10) and (11), the relationships for actuator displacements, load cell and excitation signals are determined as follows:

$$\begin{pmatrix}F_{LC1}\\F_{LC2}\end{pmatrix} = -\gamma^2\begin{pmatrix}g_{e1}&0\\0&g_{e2}\end{pmatrix}\begin{pmatrix}Z_{a1}\\Z_{a2}\end{pmatrix} + \gamma^2\begin{pmatrix}g_{e1}&b_ag_{e1}\\g_{e2}&-b_ag_{e2}\end{pmatrix}\left\{\begin{pmatrix}\frac{1}{\alpha}&0\\0&\frac{1}{\beta}\end{pmatrix}\begin{pmatrix}1&1\\b_a&-b_a\end{pmatrix}\begin{pmatrix}F_{LC1}\\F_{LC2}\end{pmatrix} + \begin{pmatrix}\frac{1}{\alpha}&0\\0&\frac{1}{\beta}\end{pmatrix}\begin{pmatrix}2c_Rs\\0\end{pmatrix}R\right\} \\ \therefore \begin{pmatrix}\alpha\beta g_{e1}&0\\0&\alpha\beta g_{e2}\end{pmatrix}\begin{pmatrix}Z_{a1}\\Z_{a2}\end{pmatrix} = \begin{pmatrix}\beta g_{e1}+b_a^2\alpha g_{e1}-\frac{\alpha\beta}{\gamma^2}&\beta g_{e1}-b_a^2\alpha g_{e1}\\\beta g_{e2}-b_a^2\alpha g_{e2}&\beta g_{e2}+b_a^2\alpha g_{e2}-\frac{\alpha\beta}{\gamma^2}\end{pmatrix}\begin{pmatrix}F_{LC1}\\F_{LC2}\end{pmatrix} + \begin{pmatrix}2c_R\beta g_{e1}\\2c_R\beta g_{e2}\end{pmatrix}sR \tag{12}$$

Using Eq. (10), the equation of the rigid beam motion is derived as follows:

$$\begin{pmatrix}m_ws^2Z_w\\j_ws^2\Phi_w\end{pmatrix} = \begin{pmatrix}-1&-1\\-b_a&b_a\end{pmatrix}\begin{pmatrix}F_{LC1}\\F_{LC2}\end{pmatrix} = \begin{pmatrix}1&1\\b_a&-b_a\end{pmatrix}\left\{\gamma^2\begin{pmatrix}g_{e1}&0\\0&g_{e2}\end{pmatrix}\begin{pmatrix}Z_{a1}\\Z_{a2}\end{pmatrix} - \gamma^2\begin{pmatrix}g_{e1}&b_ag_{e1}\\g_{e2}&-b_ag_{e2}\end{pmatrix}\begin{pmatrix}Z_w\\\Phi_w\end{pmatrix}\right\} \\ \therefore \begin{pmatrix}m_ws^2+\gamma^2g_{e1}+\gamma^2g_{e2}&\gamma^2b_ag_{e1}-\gamma^2b_ag_{e2}\\\gamma^2b_ag_{e1}-\gamma^2b_ag_{e2}&j_ws^2+\gamma^2b_a^2g_{e1}+\gamma^2b_a^2g_{e2}\end{pmatrix}\begin{pmatrix}Z_w\\\Phi_w\end{pmatrix} = \begin{pmatrix}\gamma^2g_{e1}&\gamma^2g_{e2}\\\gamma^2b_ag_{e1}&-\gamma^2b_ag_{e2}\end{pmatrix}\begin{pmatrix}Z_{a1}\\Z_{a2}\end{pmatrix} \tag{13}$$

Finally, the actuator dynamics are adequately represented by the first-order form (i = 1, 2):

$$Z_{ai} = \frac{b_a}{s+a_a} U_i \tag{14}$$

3.2.3 Derivation of the DSS controller

In Eq. (12), which represents the dynamics of Σ_N, the polynomial degrees of Z_{ai}, F_{LCi}, and R are 3, 2 and 3, respectively. This implies that in order to determine a state equation from Eq. (12), $\dot{r}$ must replace r in Fig. 7, to ensure strictly proper conditions. With the state vector set to $(z_{Na1}, z_{Na2}, z'_{Na1}, z'_{Na2}, z''_{Na1}, z''_{Na2})^T$, where $z_N = (z_{Na1}, z_{Na2})^T$ and $z_{N2} = (z'_{Na1}, z'_{Na2}, z''_{Na1}, z''_{Na2})^T$, the state equation of Σ_N, corresponding to Eq. (3), is given by:

$$\begin{pmatrix} \dot{z_{Na1}} \\ z_{Na2} \\ z'_{Na1} \\ z'_{Na2} \\ z''_{Na1} \\ z''_{Na2} \end{pmatrix} = \begin{pmatrix} a_{11} & 0 & 1 & 0 & 0 & 0 \\ 0 & a_{22} & 0 & 1 & 0 & 0 \\ a_{31} & 0 & 0 & 0 & 1 & 0 \\ 0 & a_{42} & 0 & 0 & 0 & 1 \\ a_{51} & 0 & 0 & 0 & 0 & 0 \\ 0 & a_{62} & 0 & 0 & 0 & 0 \end{pmatrix} \begin{pmatrix} z_{a1} \\ z_{a2} \\ z'_{a1} \\ z'_{a2} \\ z''_{a1} \\ z''_{a2} \end{pmatrix} + \begin{pmatrix} b_{i11} & b_{i12} \\ b_{i21} & b_{i22} \\ b_{i31} & b_{i32} \\ b_{i41} & b_{i42} \\ b_{i51} & b_{i52} \\ b_{i61} & b_{i62} \end{pmatrix} \begin{pmatrix} f_{LC1} \\ f_{LC2} \end{pmatrix} + \begin{pmatrix} b_{N1} \\ b_{N2} \\ b_{N3} \\ b_{N4} \\ b_{N5} \\ b_{N6} \end{pmatrix} \dot{r} \tag{15}$$

where a_{mn}, b_{imn}, and b_{Nm} are appropriate coefficients. From Eq. (13) and (14), and assuming the state vector is $(z_{Pa1}, z_{Pa2}, z_w, \phi_w, z'_w, \phi'_w)^T$, where $z_P = (z_{Pa1}, z_{Pa2})^T$ and $z_{P2} = (z_w, \phi_w, z'_w, \phi'_w)^T$, the state equation of Σ_P, corresponding to Eq. (5), is given by:

$$\begin{pmatrix} \dot{z_{Pa1}} \\ z_{Pa2} \\ z_w \\ \phi_w \\ z'_w \\ \phi'_w \end{pmatrix} = \begin{pmatrix} -a_a & 0 & 0 & 0 & 0 & 0 \\ 0 & -a_a & 0 & 0 & 0 & 0 \\ \frac{\gamma^2 c_{e1}}{m_w} & \frac{\gamma^2 c_{e2}}{m_w} & -\frac{\gamma^2 (c_{e1}+c_{e2})}{m_w} & -\frac{\gamma^2 b_a (c_{e1}-c_{e2})}{m_w} & 0 & 1 \\ \frac{\gamma^2 b_a c_{e1}}{j_w} & -\frac{\gamma^2 b_a c_{e2}}{j_w} & -\frac{\gamma^2 b_a (c_{e1}-c_{e2})}{j_w} & -\frac{\gamma^2 b_a^2 (c_{e1}+c_{e2})}{j_w} & 0 & 1 \\ \frac{\gamma^2 k_{e1}}{m_w} & \frac{\gamma^2 k_{e2}}{m_w} & -\frac{\gamma^2 (k_{e1}+k_{e2})}{m_w} & -\frac{\gamma^2 b_a (k_{e1}-k_{e2})}{m_w} & 0 & 0 \\ \frac{\gamma^2 b_a k_{e1}}{j_w} & -\frac{\gamma^2 b_a k_{e2}}{j_w} & -\frac{\gamma^2 b_a (k_{e1}-k_{e2})}{j_w} & -\frac{\gamma^2 b_a^2 (k_{e1}+k_{e2})}{j_w} & 0 & 0 \end{pmatrix} \begin{pmatrix} z_{Pa1} \\ z_{Pa2} \\ z_w \\ \phi_w \\ z'_w \\ \phi'_w \end{pmatrix} + \begin{pmatrix} b_a & 0 \\ 0 & b_a \\ 0 & 0 \\ 0 & 0 \\ 0 & 0 \\ 0 & 0 \end{pmatrix} \begin{pmatrix} u_1 \\ u_2 \end{pmatrix} \tag{16}$$

Finally, from Eq. (10) and (16) the interaction term $y_i = (f_{LC1}, f_{LC2})^T$, corresponding to Eq. (7), is derived as follows:

$$y_i = \gamma^2 \begin{pmatrix} -c_{e1} & 0 & c_{e1} & b_a c_{e1} & 0 & 0 \\ 0 & -c_{e2} & c_{e2} & -b_a c_{e2} & 0 & 0 \end{pmatrix} \begin{pmatrix} \dot{z_{Pa1}} \\ z_{Pa2} \\ z_w \\ \phi_w \\ z'_w \\ \phi'_w \end{pmatrix} + \gamma^2 \begin{pmatrix} -k_{e1} & 0 & k_{e1} & b_a k_{e1} & 0 & 0 \\ 0 & -k_{e2} & k_{e2} & -b_a k_{e2} & 0 & 0 \end{pmatrix} \begin{pmatrix} z_{Pa1} \\ z_{Pa2} \\ z_w \\ \phi_w \\ z'_w \\ \phi'_w \end{pmatrix}$$

$$= \gamma^2 \left\{ \begin{pmatrix} -c_{e1} & 0 & c_{e1} & b_a c_{e1} & 0 & 0 \\ 0 & -c_{e2} & c_{e2} & -b_a c_{e2} & 0 & 0 \end{pmatrix} \begin{pmatrix} -a_a & 0 & 0 & 0 & 0 & 0 \\ 0 & -a_a & 0 & 0 & 0 & 0 \\ \frac{\gamma^2 c_{e1}}{m_w} & \frac{\gamma^2 c_{e2}}{m_w} & -\frac{\gamma^2 (c_{e1}+c_{e2})}{m_w} & -\frac{\gamma^2 b_a (c_{e1}-c_{e2})}{m_w} & 1 & 0 \\ \frac{\gamma^2 b_a c_{e1}}{j_w} & -\frac{\gamma^2 b_a c_{e2}}{j_w} & -\frac{\gamma^2 b_a (c_{e1}-c_{e2})}{j_w} & -\frac{\gamma^2 b_a^2 (c_{e1}+c_{e2})}{j_w} & 0 & 1 \\ \frac{\gamma^2 k_{e1}}{m_w} & \frac{\gamma^2 k_{e2}}{m_w} & -\frac{\gamma^2 (k_{e1}+k_{e2})}{m_w} & -\frac{\gamma^2 b_a (k_{e1}-k_{e2})}{m_w} & 0 & 0 \\ \frac{\gamma^2 b_a k_{e1}}{j_w} & -\frac{\gamma^2 b_a k_{e2}}{j_w} & -\frac{\gamma^2 b_a (k_{e1}-k_{e2})}{j_w} & -\frac{\gamma^2 b_a^2 (k_{e1}+k_{e2})}{j_w} & 0 & 0 \end{pmatrix} + \right.$$

$$\left. \begin{pmatrix} -k_{e1} & 0 & k_{e1} & b_a k_{e1} & 0 & 0 \\ 0 & -k_{e2} & k_{e2} & -b_a k_{e2} & 0 & 0 \end{pmatrix} \right\} \begin{pmatrix} z_{Pa1} \\ z_{Pa2} \\ z_w \\ \phi_w \\ z'_w \\ \phi'_w \end{pmatrix} - \gamma^2 \begin{pmatrix} c_{e1} b_a & 0 \\ 0 & c_{e2} b_a \end{pmatrix} \begin{pmatrix} u_1 \\ u_2 \end{pmatrix} \tag{17}$$

Using Eq. (15), (16) and (17), all the required state variables can be obtained via numerical simulation and all the sub-matrices required for calculating Eq. (9) are directly accessible, so that the feedforward term $k_r \dot{r}$ of the controller can be determined. The feedback gain k_e was evaluated via the MATLAB *place* command, in order to locate the closed-loop pole at s = -50s^{-1}.

3.3 Test parameters

There were 3 test conditions, as shown in Table 1: parameters of a virtual primary suspension and the shaking amplitude were varied, as in the case of standard RPB tests (for finding optimal parameters). Track irregularities were chosen to be a random wave of appropriate bandwidth, with a flat velocity spectrum in the frequency from 0.1 to 3Hz, which includes the resonant frequency of the rig.

Table 1 Test conditions.

	Case 1	Case 2	Case 3
k_w (kN/m)	400	200	100
c_w (Ns/m)	400	200	100
c_R (Ns/m)	1000		

3.4 Test results

Figures 8, 9 and 10 show the shaking test results of cases 1, 2 and 3, respectively. In each time history, the observed actuator displacement followed the demand calculated via the numerical model; the corresponding synchronisation error was therefore negligible. Furthermore, in the PSD graphs there were no unexpected peak components, as shown by Fig. 4(b). Therefore, in each case, the performance of the DSS controllers was considered to be very satisfactory.

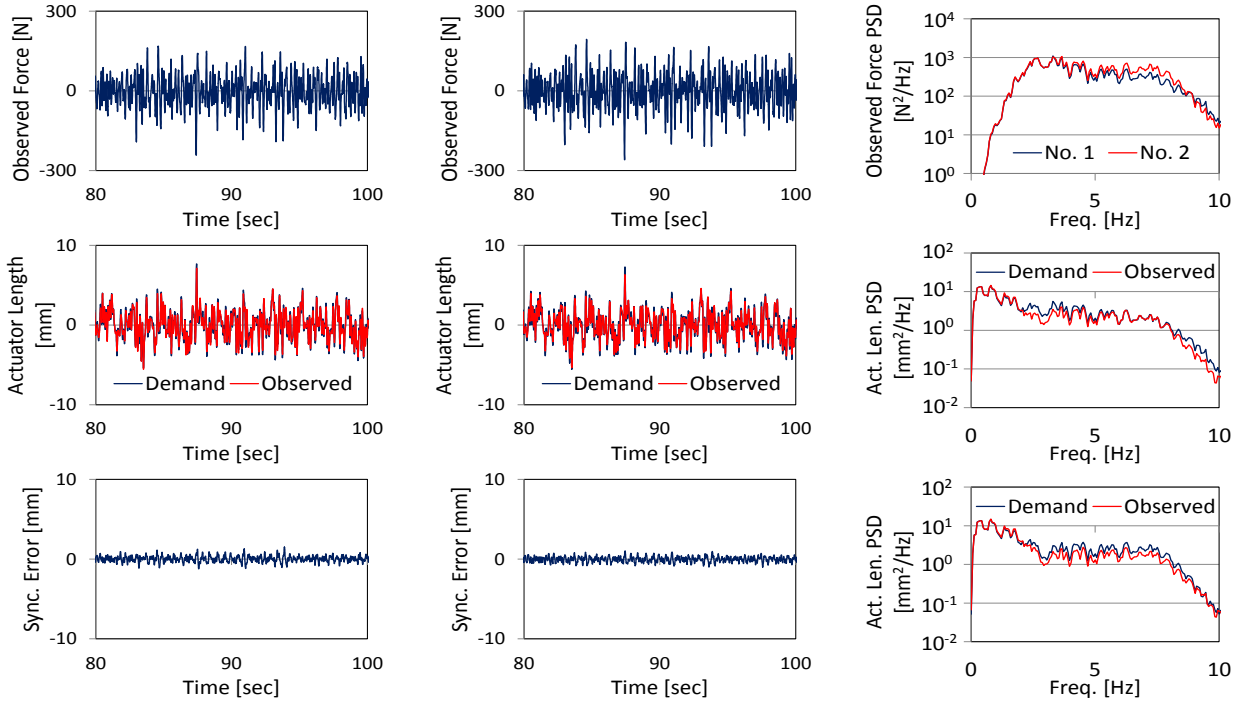

(a) No. 1 actuator response
top : observed force
middle : actuator displacement
bottom : synchronization error

(b) No. 2 actuator response
top : observed force
middle : actuator displacement
bottom : synchronization error

(c) PSD
top : observed force
middle : No. 1 actuator displacement
bottom : No. 2 actuator displacement

Fig. 8 The proof-of-concept rig test results (case 1). Both the numerical model and actual actuator displacements were well synchronised, as shown in (a), (b). There were no unexpected frequency components in (c); therefore, it could be concluded that the DSS controller worked well.

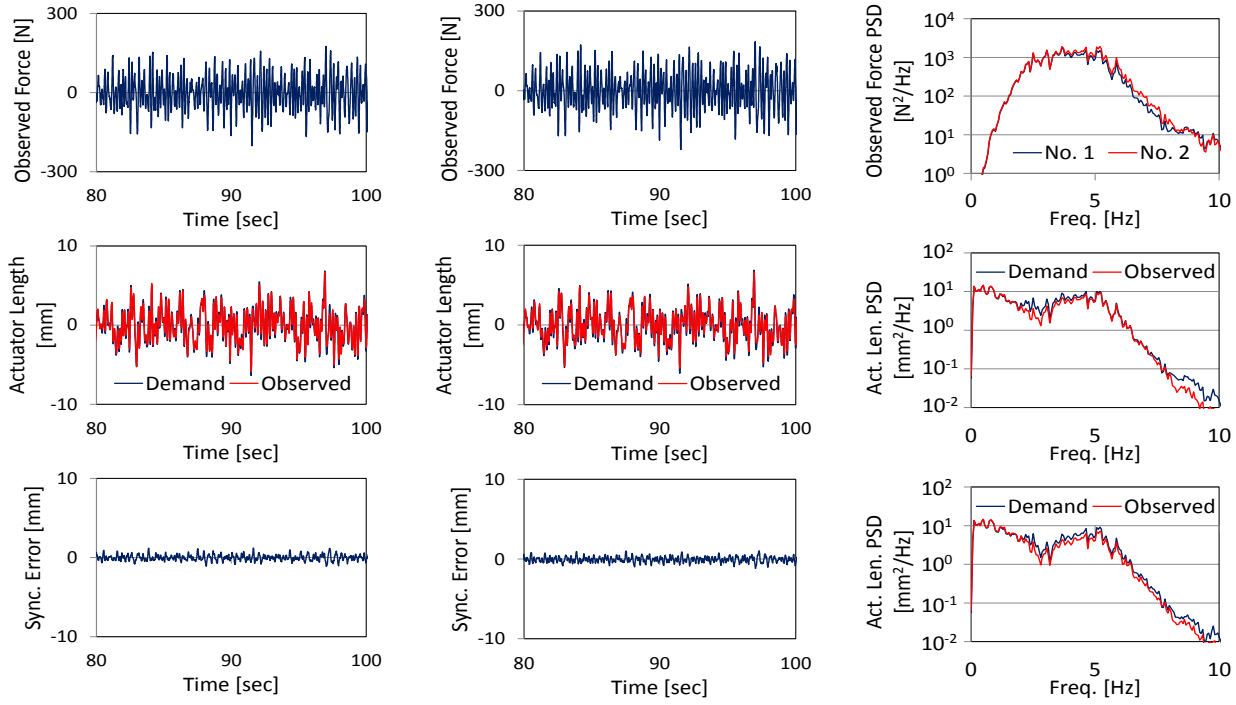

(a) No. 1 actuator response
top : observed force
middle : actuator displacement
bottom : synchronization error

(b) No. 2 actuator response
top : observed force
middle : actuator displacement
bottom : synchronization error

(c) PSD
top : observed force
middle : No. 1 actuator displacement
bottom : No. 2 actuator displacement

Fig. 9 The proof-of-concept rig test results (case 2). Both the numerical model and actual actuator displacements were well synchronised, as shown in (a), (b). There were no unexpected frequency components in (c); therefore, it could be concluded that the DSS controller worked as well as the DSS controller for case 1.

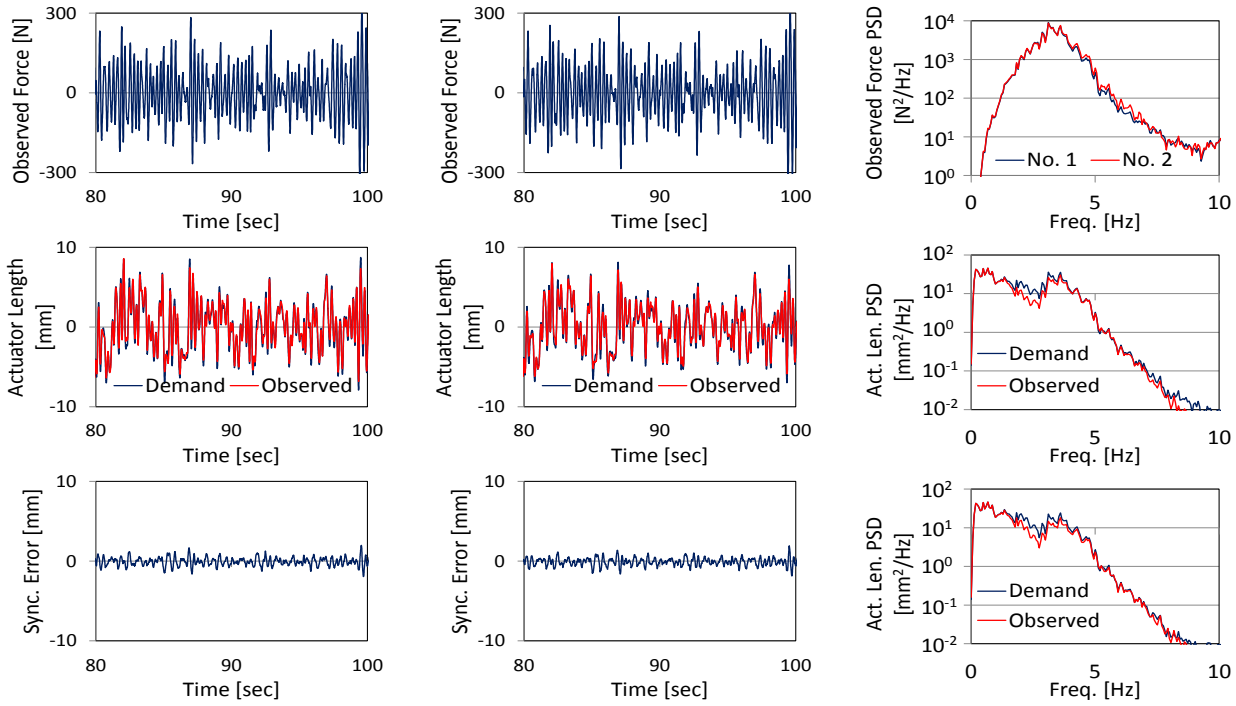

(a) No. 1 actuator response
top : observed force
middle : actuator displacement
bottom : synchronization error

(b) No. 2 actuator response
top : observed force
middle : actuator displacement
bottom : synchronization error

(c) PSD
top : observed force
middle : No. 1 actuator displacement
bottom : No. 2 actuator displacement

Fig. 10 The proof-of-concept rig test results (case 2). Both the numerical model and actual actuator lengths of each actuator were well synchronised, as shown in (a), (b). There were no unexpected frequency components in (c); therefore, it could be concluded that the designed DSS controller worked as well as the DSS controllers for cases 1 and 2.

However, the originally derived feedback gain k_e was too found to be too large, with a potential for inducing instability. Therefore reducing its value empirically was found to be necessary. The reason for this was probably due to sensor noise propagation due to the relatively high bandwidth design of the closed-loop pole at s = -50s^{-1}. This suggests the need for a stochastic DSS analysis as an aspect of future work.

4. Discussion

We have shown that the proposed DSS controllers were effective in terms of synchronisation between numerical model and actual actuator displacements. In this section, we briefly compare the previous experimental results with simplified simulation results.

Assuming that the characteristics of the rig are perfectly known and that each actuator tracks its demand perfectly, then $z_{ai} = u_i$. In this case, the rig beam never rotates and its motion will be the same as the motion of the simplified model shown in Fig. 11. In this model, Eq. (18), (19) and (20) can be derived; therefore the transfer function from the excitation signal to the actuator displacement is as written in Eq. (21). Note that capital letters in Eq. (3) ~ (6) represent Laplace-transformed variables shown in Fig. 11.

$$F_{LCi} = -\gamma^2 g_{ei} Z_{ai} + \gamma^2 g_{ei} Z_w \tag{18}$$

$$\frac{1}{2}(m_w s^2 + c_w s + k_w) Z_w = C_R s R \tag{19}$$

$$F_{LCi} = -\frac{1}{2} m_w s^2 Z_w \tag{20}$$

$$\frac{Z_{ai}}{sR} = \frac{C_R}{\gamma^2 g_{ei}} \frac{(m_w s^2 + 2\gamma^2 g_{ei})}{(m_w s^2 + c_w s + k_w)} \tag{21}$$

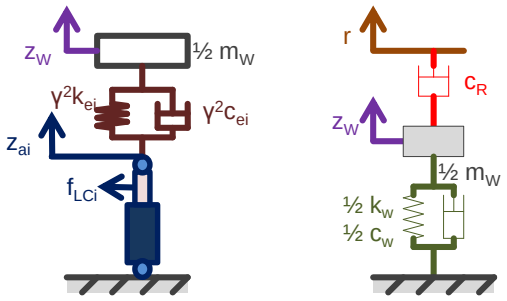

(a) Rig (b) Emulation model

Fig. 11 Simplified rig and emulation model. Assuming well-known parameters and an ideal response of the actuator, the mass motion of the proof-of- concept rig is restricted to the vertical direction in this simple study.

Figure 12 shows the PSD comparison between the measured actuator displacements and the derived ones from Eq. (21). The PSDs are sufficiently close to one another and we conclude that the designed DSS controllers performed well. However, these tests are effectively restricted to linearisable conditions. One of the most important advantages of DSS testing is the improved understanding of unmodelled phenomena, such as nonlinearity, using actual components. Therefore, testing under more severe conditions will also be the subject of future work.

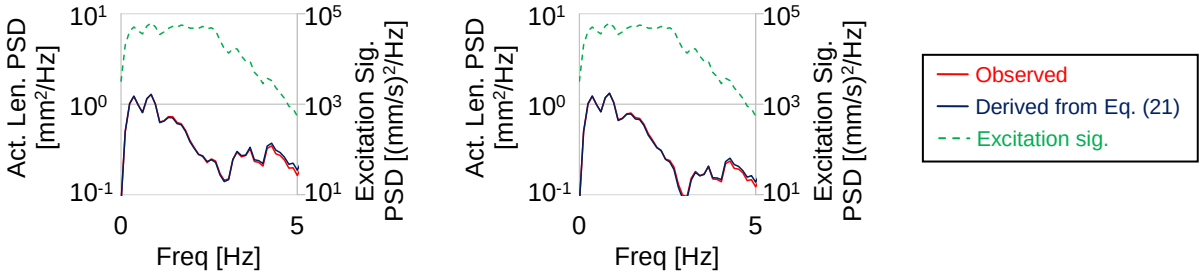

(a) No. 1 Actuator (b) No. 2 Actuator

Fig. 12 Comparison between experiment and numerical result of case 1. Both coincided with each other over the excitation frequency range.

5. Conclusions

In this paper, a DSS strategy to improve the RPB actuator control performance was introduced. The main conclusions are as follows:

A) A state-space DSS approach was adopted for application to the combination of the existing proof-of-concept rig and a demonstrator model.
B) Using the rig, shaking tests were conducted and the actuator displacements were well-synchronised with their corresponding numerical models demands. No unexpected motions, which were seen in the original RPB tests at RTRI, were observed.
C) Application of parameter variations to the tests, using three different virtual suspension parameter sets, resulted in the DSS controllers exhibiting the same degree of excellence in closed-loop performance.
D) As a consequence, the DSS approach was determined as a viable framework for future research on the RPB system, from the viewpoints of (1) avoidance of the deterioration of control performance caused by dynamic coupling and (2) straightforward parameter changeability of virtual devices.

Appendix

Notations and parameters

Parameter	Description	Value		
Fixed parameters				
m_w	Mass of rigid body beam / wheelset	172 kg		
j_w	Moment of inertia about beam / wheelset	94 kg m^2		
k_{e1}, k_{e2}	Suspension spring constants	210 kN/m, 244 kN/m		
c_{e1}, c_{e2}	Suspension damping constants	5560 N s/m, 5600 N s/m		
$2b$	Distance between virtual creep dampers	1 m		
$2b_1$	Distance between suspensions	1.3 m		
$2b_p$	Distance between pivots of swing-arms	1.1 m		
$2b_a$	Distance between actuators	1.7 m		
c_r	Damping constants of virtual creep dampers	1000 N s/m		
Variable parameters		Case 1	Case 2	Case 3
k_w	Sum of spring constants of virtual primary suspensions	400 kN/m	400 kN/m	400 kN/m
c_w	Sum of damping constants of virtual primary suspensions	400 N s/m	400 N s/m	400 N s/m

Abbreviations

DSS	dynamically substructured systems
LVDT	linear variable differential transformer
PSD	power spectral density
RPB	rapid prototyping bogie
RSTP	rolling stock test plant

References

Morishita, H., Sasaki, K., Shimomura, T. and Watanabe, N., Development of a Variable Characteristics Test Truck, Proceedings of J-Rail2010 (2010), pp.165–168 (in Japanese).

Stoten, D. P. and Hyde, R. A., Adaptive control of dynamically substructured systems: the single-input single-output case, Proceedings of the Institution of Mechanical Engineers, Part I: Journal of Systems and Control Engineering, Vol.220, No.2 (2006), pp.63-79.

Stoten, D. P., Tu, J. Y. and Li, G., Synthesis and control of generalized dynamically substructured systems, Proceedings of the Institution of Mechanical Engineers, Part I: Journal of Systems and Control Engineering, Vol.223, No.3 (2009), pp.371-392.

Tu, J. Y., Stoten, D. P., Li, G. and Hyde, R. A., A state-space approach for the control of multivariable dynamically substructured systems, Proceedings of the Third IEEE Conference on Systems and control (2009), pp. 1093-1098.

Watanabe, N., Sasaki, K., Koganei, R. and Morishita, H., Fundamental Tests on a Rapid Prototype Bogie, Quarterly Report of RTRI, Vol.53, No.4(2012), pp.199-204.